Shap. Mem. Superelasticity
https://doi.org/10.1007/s40830-024-00481-1

ORIGINAL RESEARCH ARTICLE

Temperature-Controlled Laser Processing of Shape Memory Wires: Spherical Ends as Connectors for System Integration

Marvin Schuleit[1] · Yunus Kutlu[1] · Burkhard Maaß[2] · Nicole Stötzel[3] · Jan Frenzel[3] · Cemal Esen[1] · Gunther Eggeler[3] · Andreas Ostendorf[1]

Received: 14 February 2024 / Revised: 5 March 2024 / Accepted: 6 March 2024

Abstract Nickel–Titanium-based shape memory alloys have reached a high technological relevance in the medical field and also for actuation/energy conversion. At present, the interest in new actuation solutions is steadily increasing. However, one important challenge for the design of new actuators is the lack of connection and coupling options, which often hinders a reliable system integration. To address this challenge, this study presents a temperature-controlled laser processing approach for the generation of spherical ends on shape memory wires, which allow a relatively simple integration into different types of systems (e.g., printed circuit boards) in a form-fitting manner. For this purpose, an experimental setup with an integrated pyrometer was used to establish spherical ends on thin NiTi wires with a diameter of 0.24 mm. The resulting microstructures and the functional properties were investigated using scanning electron microscopy, thermal analysis, uniaxial tensile testing, actuation fatigue testing, and hardness measurements. The results obtained in the present study indicate that our laser procedure successfully yields reliable connection options for NiTi wires, without harming the functional performance of the material.

Keywords SMA · NiTi · Cyclic stability · Fatigue · Mechanical behavior · Transformation temperature

✉ Marvin Schuleit
marvin.schuleit@rub.de

[1] Applied Laser Technologies, Ruhr University Bochum, Universitaetsstrasse 150, 44801 Bochum, Germany

[2] Ingpuls GmbH, Von-Waldthausen-Straße 77, 44894 Bochum, Germany

[3] Material Science and Engineering, Ruhr University Bochum, Universitaetsstrasse 150, 44801 Bochum, Germany

Introduction

Shape memory alloys (SMAs) exhibit exceptional actuator and sensory functionalities utilized in various industrial sectors, such as medical technology, aerospace, and automotive [1–4]. In these fields, where lightweight, silent operation and high performance are crucial requirements, they are gaining increasing significance. SMAs can be exploited as actuators with minimal additional components, resulting in weight and space savings compared to electromagnets. Commercially wrought SMAs are available in the form of wires, foils, sheets, and tubes. Wires with various thicknesses and distinct shape memory effects (SMEs) are readily available on the market. Despite attempts by the industry to establish standardized actuators, numerous customized actuator systems are being developed. In the case of actuators, Nickel–Titanium (NiTi) is predominantly used due to NiTi's superior SMEs. The underlying mechanism for the SMEs is the reversible martensitic transformation, where the high-temperature phase austenite transforms into the low-temperature phase martensite on cooling/mechanical loading. Upon heating/unloading, the reverse transformation takes place. In most actuation applications, the extrinsic two-way effect is exploited, in which a constant force is applied and the phase transformation is triggered by heating, thereby realizing actuator movement. System integration of SMA wires often involves a firmly bonded or clamped connection (e.g., casting, crimping, adhesive bonding). However, these techniques have significant drawbacks. The intensity of the SME and the fatigue life of the actuator strongly depend on microstructure and surface condition [5–9]. Therefore, exposing the material to elevated temperatures or mechanical stresses/surface damage during processing can affect actuator performance. Moreover, conventional connections cannot be undone without causing harm to the actuator. Adhesive joints require additional surface treatments and the mechanical

Published online: 23 April 2024

compatibility of these joints can be problematic [10–13]. Especially, the incorporation of wire actuators into engineering systems necessitates additional developmental steps as compared to standardized and pre-assembled actuators. To address these challenges, a novel approach based on a form-fit connection is investigated in the present study. The approach consists of melting the ends of conventional SMA wires to establish a sphere, which, due to its larger diameter, can be used as a form-fit connection element. In the present work, an experimental setup with an integrated high-speed pyrometer was used to control the surface temperature of the melt pool during sphere generation. A first proof of concept applying this technique without temperature control has already been published elsewhere [14]. As an application example for such actuators with spherical ends, a connection to a printed circuit board can be realized by press-fitting the manufactured spherical end into a coated hole, providing a mechanical anchorage and an electrical connection. In general, lasers are important tools for processing and welding NiTi SMAs since they apply the energy locally at high densities and thus minimize the size heat-affected zones, HAZs [14–19]. However, the successful laser processing of NiTi strongly relies on precise control of process temperatures. Particularly with smaller material volumes, such as wires, the risk of uncontrolled overheating exists, as the usage of constant laser power does not provide control of the temperature due to the high process dynamics. This may lead to unintentional vaporization of nickel, which has a significantly lower vaporization temperature of 2730 °C compared to the vaporization temperature of titanium with 3260 °C [20]. Alternatively, there are different material characteristics, such as microstructure and transformation behavior, which are strongly dependent on the thermal history of the material. Modern pyrometers allow real-time monitoring and control of temperatures, preventing excessive heat accumulation and potential material damage. In scientific research and comparative studies, the inclusion of an advanced pyrometer enhances the consistency and reliability of experimental data [21–24]. Researchers can establish a standardized framework for assessing laser processing parameters by precisely measuring and documenting process temperatures, facilitating meaningful comparisons, and promoting reproducibility across different studies. The present work addresses the performance of temperature-controlled fused spherical shape memory wire actuators in terms of mechanical, thermal, and functional properties.

Experimental Section

Material

In this investigation, binary NiTi wires with a nickel content of 49.8 at.% and a diameter of 0.24 mm, obtained from Ingpuls GmbH, were employed as the experimental material. The wires underwent a comprehensive surface cleaning procedure to remove the surface oxide layer and remaining residues. Involving a 10-min ultrasonic cleaning in ethanol, followed by etching for 10 min at 60 °C in commercially available TitanEtch from Titantech Europe (mixture of sodium fluoride, ammonium persulfate, and distilled water) and a final 10-min ultrasonic cleaning in ethanol. Subsequently, the wires were stored in ethanol to minimize surface contamination prior to further processing.

Characterization of the Fused Spherical Shape Memory Wire Actuators

The geometric characterization of a preliminary study was performed with a TM-006 optical micrometer from Keyence Deutschland GmbH and an additional rotation axis equipped with a stepper motor. The geometrical dimensions could be completely determined by rotating the sphere actuators by 360° and simultaneously measuring their dimensions. The mechanical properties of the material were assessed through uniaxial tensile testing and microhardness measurements at room temperature. Uniaxial tensile tests were performed on a FMT 310 from Alluris GmbH & Co. KG with a load cell of 50-N crosshead speed of 1 mm/min to test wire samples with one sphere on the wire end to investigate their response to an applied load. During the experiment, the sphere is kept in position by a holder with a chamfered hole and the wire end is clamped by a screw connection. Microhardness measurements were conducted on the cross-sections of the sphere wire end using a Carat 930 from ATM Qness GmbH. As a result of the applied force exerted by the indenter, the material undergoes detwinning. Therefore, one has to note that the obtained data only represent "apparent hardness values." A normalization process was applied in order to analyze the hardness properties in terms of comparability within this study. To characterize the material's transformation behavior, differential scanning calorimetry (DSC) measurements were employed on a DSC 204 F1 from Erich NETZSCH GmbH & Co. Holding KG. DSC analysis encompassed the unstrained wire as well as the processed spheres to examine any alterations induced by the laser process. For the purpose of microstructural characterization, the specimens were ground, polished, and then exposed to an etchant (50 ml of Beraha-I solution with 15 g of ammonium difluoride) in order to visualize the grain structure with an optical microscope of type Axio imager A1m from Carl Zeiss Microscopy Deutschland GmbH. Polarized light was used to obtain good contrast. The fracture surfaces of the specimens were examined using scanning electron microscopy (SEM) EVO MA10 from Carl Zeiss Microscopy Deutschland GmbH. By employing these combined methodologies, a comprehensive understanding of the material's mechanical properties,

transformation behavior, microstructure, and fracture characteristics was achieved. For the functional characterization, actuators with spheres at both ends were fabricated and pressed into through-hole plated boards from JLCPCB GmbH. The actuator wire length from sphere bottom to sphere bottom was 51 mm. These assemblies were subsequently integrated into a test rig, Fig. 1, and subjected to cyclic loading. The test rig was located in an air-conditioned laboratory at a temperature of 21 °C ± 1 °C. The current was applied for a total duration of 3 s, utilizing a linear ramp for 2.7 s until reaching the target current of 0.875 A with a subsequent plateau of 0.3 s. Within this heating phase, the wire transforms from martensite to austenite and generates actuating stroke. Subsequently, the current is reduced and kept at a low level (cooling phase) and the wire transforms to martensite and elongates due to the force applied by the spring. To replicate the service life of such an actuator, the process is repeated cyclically. The applied stress was set at 300 MPa, with an initial strain of 4%, achieved by employing a low *c*-value tension spring to maintain a nearly constant load within the displacement range. The displacement was accurately monitored using object tracking based on the Opencv library. For this purpose, a marker is placed on a printed circuit board and its movement is tracked with the assistance of a camera. Cyclic testing under constant load induces functional fatigue, with long-term implications for the formation and propagation of cracks. In literature, this fatigue phenomenon is often referred to as "actuation fatigue" [25–28]. The specimens were subjected to cyclic loading until failure occurred, allowing for precise localization of the failure site. SEM imaging further provided valuable insights into the underlying fracture mechanisms of the cyclically tested actuators.

Setup

The experiments were conducted on a 3-axis numerically controlled workstation equipped with an Yb-fiber laser redPOWER® QUBE from SPI Lasers, operating with an emission wavelength of 1075 nm ± 7 nm. The experimental setup with the optical paths is shown in Fig. 2. The laser beam is guided to the process head by an optical fiber with a core diameter of 100 µm and then collimated with a lens (L1, focal length 114 mm). Subsequently, the beam is vertically deflected with a dielectric mirror (DM1) and finally focused on the wire end with a lens (L2, focal length 150 mm). To visualize the process for improved positioning, a second dichroic mirror (DM2) was employed to reflect the visible electromagnetic radiation path toward a mirror (M) and eventually to a camera (Cam). The heat radiation generated from the top of the fusion zone was collimated by L2, transmitted through DM2, and then focused with a lens (L3) onto a fiber-optic cable. This cable led to a high-speed two-color pyrometer, Metis H322 from Sensortherm GmbH with a temperature range from 700 to 2300 °C, equipped with an integrated PID controller and two detectors operating at 1.45–1.65 µm and 1.65–1.8 µm. The pyrometer was connected to a PC for data acquisition and also directly linked to the laser to establish a closed control loop with minimal latency. The pyrometer was calibrated using a portable heat

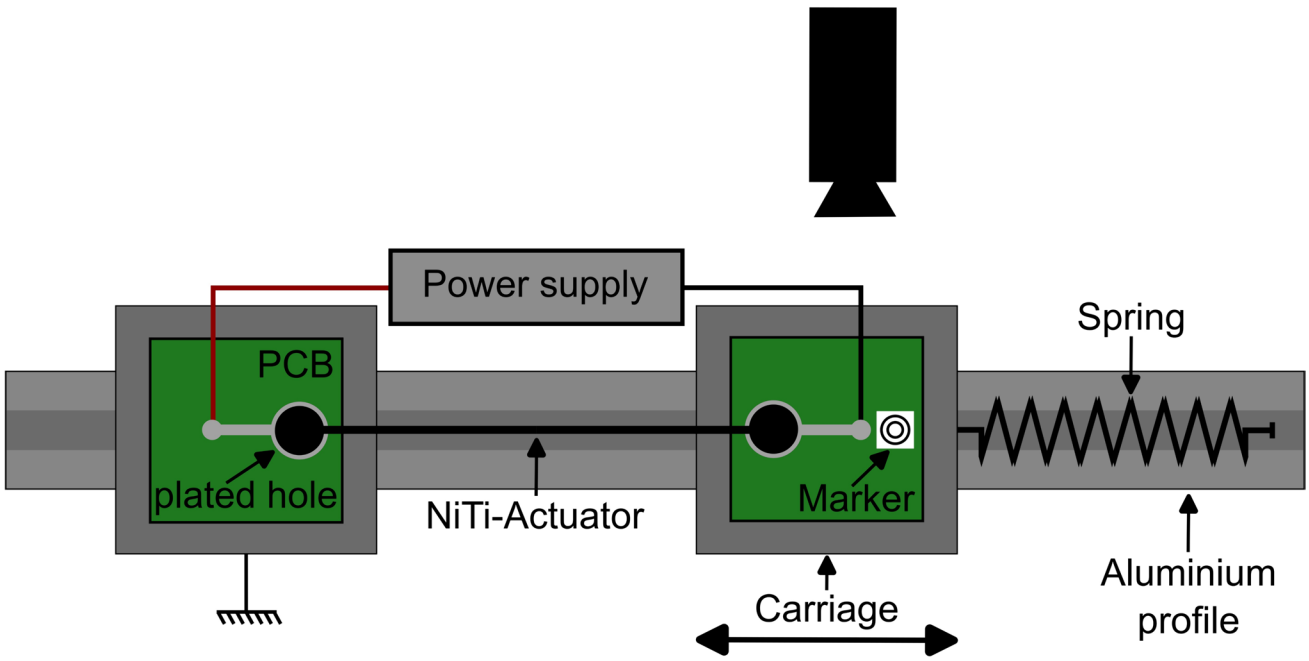

Fig. 1 Schematic illustration of the setup for fatigue life testing

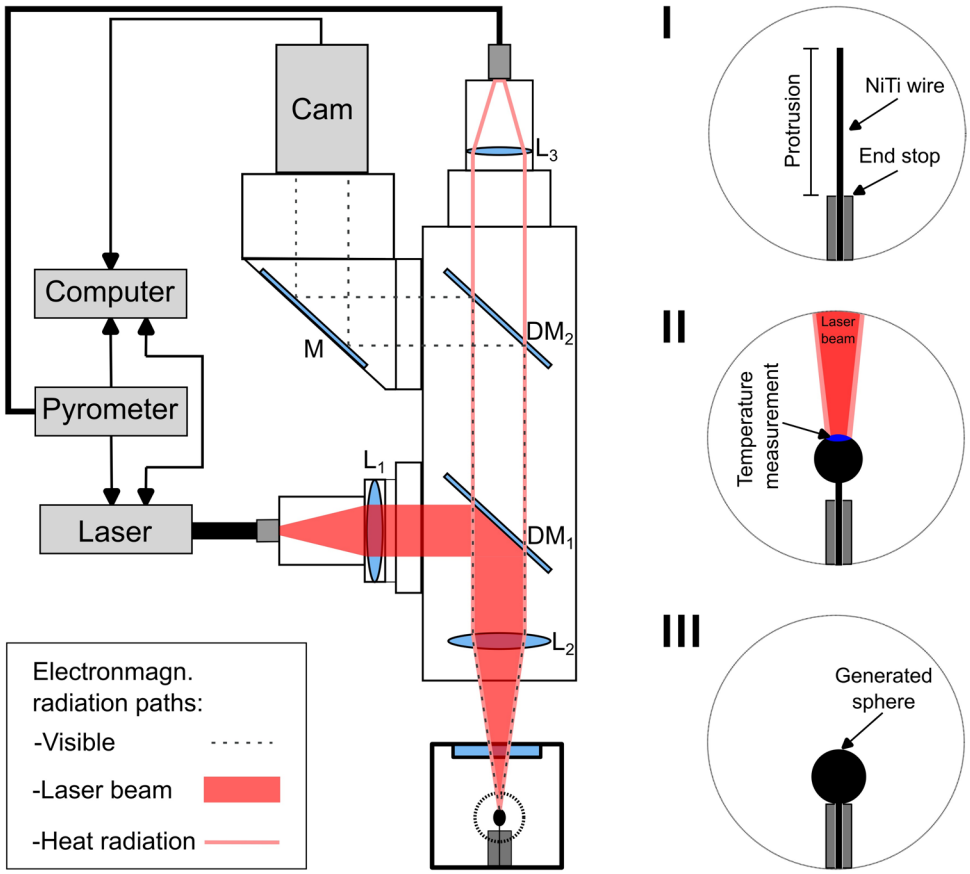

Fig. 2 Experimental setup for temperature-controlled laser processing of actuators with spherical ends. I–III visualize the conditions before, during, and after the manufacturing process

source HE1200 from Sensortherm GmbH to compensate for the optical losses caused by different optics. An emissivity ratio of 1 was selected for the experiments. To manufacture the fused spherical shape memory actuators, a NiTi wire was placed in a process chamber using a clearance fit. The protrusion had a defined length of 10 mm. The chamber was filled with argon gas to minimize oxidation during processing. The laser was focused on one wire end to heat the material beyond its melting temperature of 1310 °C [29]. A spherical shape was formed at the wire end during the process, owing to the energetic-efficient ratio of surface to volume. The upper plane of the holder with the clearance fit serves as a sphere end stop.

The seamless integration of the spheres into the circuit board necessitates that the spheres maintain a consistent diameter throughout the form-fit connection. In previous tests without control, the manufactured spheres showed varying diameters, which made it impractical to attach a variety of actuators. As the process is not controlled, the process temperatures vary and may overheat causing additional material below the end stop to be drawn into the melt pool. Measured temperature curves are provided in a Supplementary File. For actuator applications, this means counterproductive variations in actuator length, which can only be compensated for to a limited extent depending on the installation scenario. To improve production consistency and comparability, the temperature was kept constant using the pyrometer and the integrated PID controller. The optimum temperature was determined with a temperature screening. Table 1 lists the average generated sphere diameter without temperature control and with temperature control at 1800 °C and 2100 °C. A consistently melted NiTi wire end with a spherical shape was achieved with a target temperature of 1800 °C of the pyrometer-based laser power control and a total processing time of 3 s. Below 1800 °C, either the amount of material for a sphere with a diameter of 0.94 mm was not entirely fused or shape defects and kinking of the wire occurred. The Supplementary File provides images of these defects. The lowest stable process temperature was selected for the presented study to minimize the amount of thermal input. While the temperature difference between the set process temperature of 1800 °C and the melting point

Table 1 Average generated sphere diameter without temperature control and with temperature control (1800 °C, 2100 °C; $n = 5$)

	Without temperature control	1800 °C	2100 °C
Diameter (mm)	1.015 ± 0.1	0.939 ± 0.007	1.000 ± 0.045

of 1310 °C may initially seem counter intuitive, it can be plausibly explained by the fact that the laser and the temperature measurement are exclusively focused on the top part of the specimen. The applied laser radiation is absorbed, converted to heat, and subsequently, heat conduction leads to the melting of segments in close proximity to the absorption zone. As a result, the molten NiTi strives to reduce its surface energy and thus forms a sphere. With this formation of a sphere, a temperature gradient is to be expected since the melt pool temperature reaches its maximum in the laser absorption zone, whereas the bottom part solely melts through heat conduction. Thus, in this setup a temperature needs to be selected with exceeds the melting point in order to generate a sphere of a specific size. Initial PID coefficients were determined using a heuristic approach and iteratively adjusted until a satisfactory convergence with the target temperature was consistently attained.

Results and Discussion

The laser-based treatment leads to the formation of a uniform sphere with a diameter close to 0.94 mm, illustrated in Fig. 3a. The sphere is located centrally on the wire and features a conical transition from sphere to wire. On the top of the sphere no indication of elevated process temperatures, such as an unsealed keyhole or spatter, can be observed. Figure 3b visualizes the controlled temperature profile while processing the wire end. The target temperature of 1800 °C is reached within a few ms and displays minor fluctuations initially toward lower temperatures. These are attributable to the dynamically moving melt pool, the orientation of the melt pool and the small melt volume at the beginning. An overshooting to higher process temperatures could not be detected. The target temperature stays constant for the remaining process time without significant temperature variations. Subsequently, the sample cools down over several hundred ms until the minimum measuring temperature of 700 °C is reached.

Microstructure and Phase Transformation

Due to the complete melting of the wire end, a modification of the microstructure was expected. Figure 4a shows the microstructure inside the sphere. A cast-like arrangement of columnar grains oriented parallel to the main heat flow direction can be seen. The lengths of these grains varied between 150 and 415 µm. We note that these grains represent prior austenite grains, which were revealed through the etching procedure. The type of color etchant which was used in the present study is known to mainly provide microstructural information related to the high-temperature phase in NiTi (as documented in previous publications [30, 31]). A close look into the inner parts of the prior austenite grains allows to detect needle-like martensitic features. However, these details only appear with weak contrast. An effort was made to optimize the visibility of these microstructural features using further image processing. The corresponding graphical representation is contained in the supplement of this publication. Moving from the laser-generated sphere toward the other parts of the wire, one can observe a transition from large columnar grains to smaller equiaxed grains. In this transition zone, grain sizes varied between 14 and 59 µm. In this region, where material was not melted, the alloy has been exposed to high process temperatures, which resulted in a localized heat treatment, Fig. 4b. Finally, the microstructure of the original base material is presented in Fig. 4c. The corresponding optical micrograph shows the presence of small regions (close to a few micrometers) with different contrasts, which could be interpreted as prior austenite grains in the unaffected wire. However, it is very likely that actual grain size in this region is significantly below

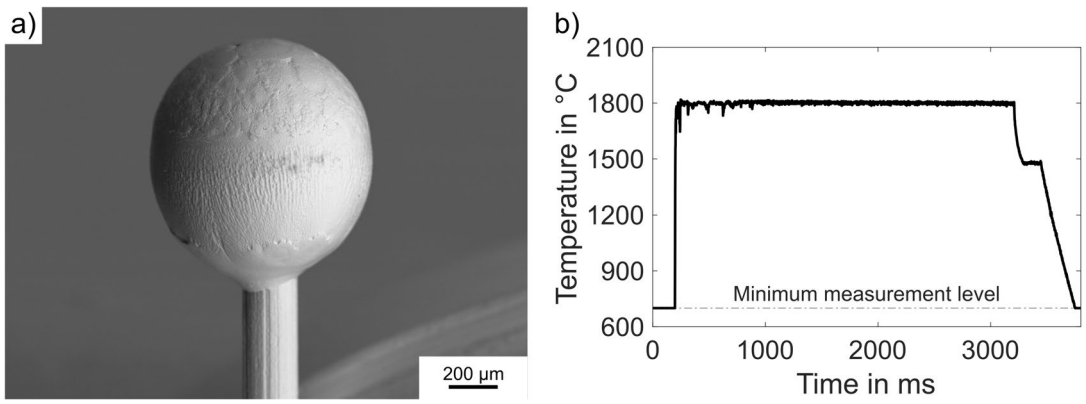

Fig. 3 Temperature-controlled laser processing: **a** SEM image of a wire end with a generated sphere processed at 1800 °C and **b** temperature profile during manufacturing of a sphere using closed control loop

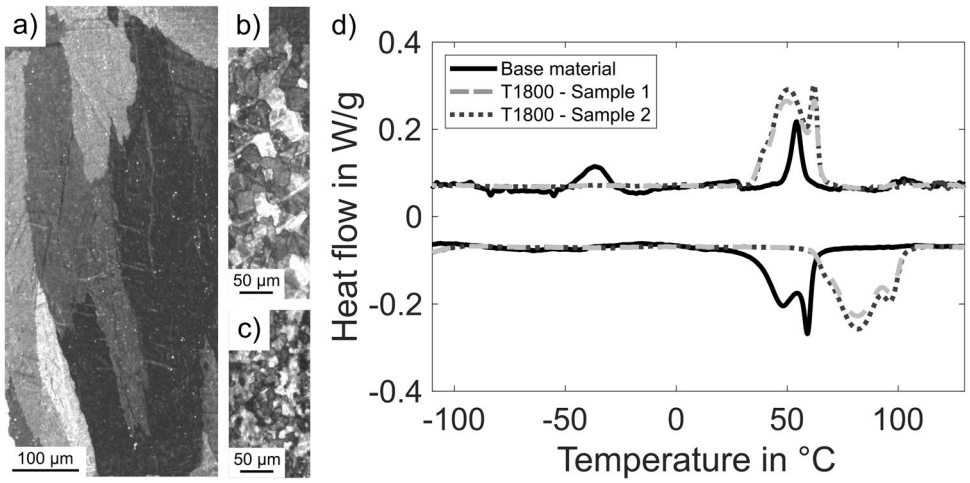

Fig. 4 Microstructure and transformation behavior: **a** cast-like structure with elongated columnar grains, **b** enlarged equiaxed grains in the heat-affected zone, **c** nanocrystalline grains in the base material, and **d** DSC-measurements of the base wire material and manufactured spheres

1 µm [8], such that these features cannot be resolved in the optical micrograph.

In a next step, it was analyzed how laser processing alters the phase transformation behavior of the SMA wire. Figure 4d presents three DSC curves which are related to the base material prior to laser processing (black solid line) and to two laser-generated spheres (dotted/dashed gray lines). Each DSC chart consists of a cooling segment (positive heat flow) and of a heating segment (negative heat flow). The unprocessed base material shows two widely separated peaks on cooling which indicate the formation of R-phase (between 59.4 and 48.2 °C) and of B19′ martensite (between − 24.7 and − 54.4 °C). The reverse transformations occur on heating, whereas both types of transformations, B19′ martensite → R and R → B2 austenite, occur in a smaller temperature range as compared to the cooling cycle. The overall behavior presented in Fig. 4d for the base material is generally common for NiTi SMAs with nanocrystalline grain structures, e.g., References [9, 32]. For the scope of the present work, it is important to understand that the base material shows the R-phase at room temperature in the absence of external stresses. During functional testing, however, where the wire is subjected to heating and cooling, high stresses promote the formation of B19′ martensite. Laser melting significantly affects phase transformation behavior. The two datasets obtained form laser-generated NiTi spheres both show overlapping two-step-transformations on heating and cooling. This type of transformation behavior has been previously reported for NiTi powders of similar composition which were rapidly solidified in a gas atomization process [33]. This behavior is likely caused by small-scale chemical heterogeneities which evolve during solidification and probably by the presence of solidification-related stresses. As shown in Fig. 4a, the remelted sphere shows significantly larger prior austenite grains, which explains why the final reverse transformation in the remelted spheres occurs at higher temperatures on heating as compared to the original base material. Further work is required to rationalize these findings. The DSC curves of the two laser processed materials states (labeled T1800: Sample 1 and T1800: Sample 2) are characterized by higher martensite finish temperatures on cooling (close to 36 °C). Therefore, the material is in the martensitic state, after cooling down to room temperature after laser processing.

Mechanical Properties

The stress–strain diagram of three fabricated specimens is presented in Fig. 5a. The stress initially exhibits a more or less linear increase, followed by a transition to a stress plateau at 210 MPa, maintained up to 8% strain. Subsequently, the material undergoes plastic deformation until failure, observed at 942 MPa ± 12 MPa and around 20% strain. The hardness measurements reveal three distinct regions, illustrated in Fig. 5b. The first three bars represent data which were obtained after the wire (including base material, sphere, and HAZ) was cooling down to room temperature after processing. The data in Fig. 5b show that the base material apparently has the highest hardness compared to the other zones. This finding is mostly related to the fact that different phases are present in the three different regions. From DSC chart in Fig. 4d one can conclude that after cooling down to room temperature, the sphere and the HAZ are mostly in the martensitic state. In contrast, the base material is characterized by the presence of R-phase. This situation is associated with different elementary deformation mechanisms during hardness measurements. While indentation in the sphere and in the HAZ involves detwinning of B19′ martensite, the base material first needs to form stress-induced B19′ martensite during mechanical loading. This probably yields a higher hardness value. This assumption was confirmed after cooling the specimen down in liquid nitrogen for one minute. This procedure establishes the presence of B19′ martensite in the base material. The corresponding

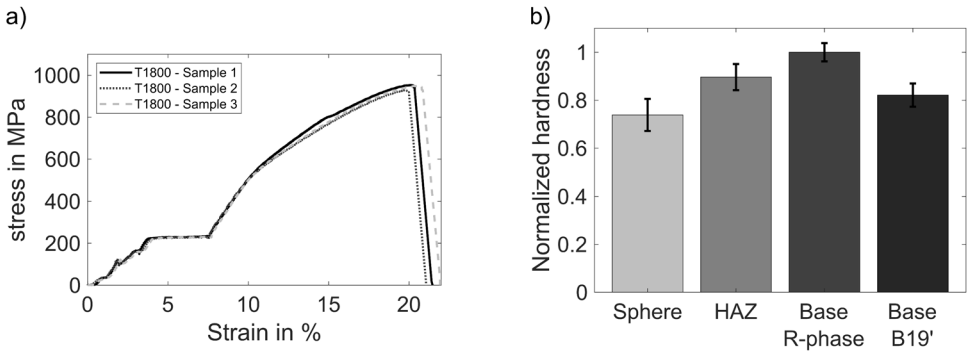

Fig. 5 Mechanical data from tensile and hardness testing: **a** stress–strain curves and **b** hardness levels in different areas

hardness value of this region (fourth bar in Fig. 5b) is now close to what has been measured for the other wire regions in the martensitic state. Demonstrating that the strong microstructural changes (Fig. 4a) associated with laser processing do not provide a strong direct effect on hardness values. The corresponding microstructural changes, moreover, affect the presence of R-phase and B19′, which results in an indirect effect on hardness values. The mechanical properties align with the microstructure and the failure location, approximately 300–400 µm below the sphere, as depicted in Fig. 6a–d along with the corresponding fracture surfaces. SEM images depict a necking phenomenon in this region. The melting process leads to grain coarsening within the sphere and in the HAZ, as shown before. Consequently, the material starts to deform plastically at lower stress levels. Ultimately, a cup and cone fracture occurs, exhibiting a dimple structure, a common characteristic of ductile materials [34]. The achieved strength is reduced in comparison with the base material with a tensile strength of 1300 MPa, but is more than twice as high as typical stress levels in actuator applications with 200–400 MPa.

Functional Properties

Characterization of the properties over the service lifetime is crucial for subsequent actuator applications and has remained an important area of research [5, 34–41]. Fundamentally, a distinction is made between functional fatigue and structural fatigue. Functional fatigue describes the decrease in functional properties, typically the actuator strain. Structural fatigue addresses the formation and propagation of cracks under cyclic loads, which ultimately lead to structural failure [42]. Figure 7a illustrates the strain behavior over the service life of three PCB sphere actuators transformed by resistance heating. All three tested actuators show a significant strain reduction within the first few hundred cycles, which decreases with increasing cycles and converges asymptotically to a constant value until failure. Figure 7b shows the change in the resistance profile during the first 500 cycles for Sample 1. The resistance within one cycle increases in the first 2.5 s until the transformation to austenite starts and the resistance decreases. Similar behavior has also been reported in the literature [43–46]. The resistance profiles during the heating phase show a decrease in resistance with increasing cycles for the three actuators, exemplified for Sample 1 in Fig. 7b. The origin of the reduction in resistance requires a more detailed investigation since there have also been reports of increasing resistance in the literature [36, 46]. The significance of laser processing in this regard cannot be quantified at this stage, since a similar resistance reduction was also observed in cyclic testing of the base material. The strain response of the three tested actuators is in principle similar, but not identical. Sample 2 demonstrates a more constant strain level after only 300 cycles. Sample 1 shows such a range at a similar point in time; however, after a few hundred cycles the strain decreases again considerably and then only stabilizes at a nearly constant value after approximately 2000 cycles. Sample 3 achieves stabilized strain behavior after more than 2000 cycles. The observed variations in functional performance can be explained by ambient conditions fluctuations. Despite the experiments being conducted within a climate-controlled environment, the potential for temperature fluctuations of up to 2° persists. The base material, which is mostly present in a manufactured actuator, has a narrow temperature range in which the austenitic transformation occurs (Fig. 4d) and with the current settings used, no complete transformation takes place. As a result, small temperature changes can have a significant effect on the strain behavior. The varying service life of the three samples shown is presumably caused by different pronounced localized surface defects resulting from the wire manufacturing process, which is further discussed in section structural fatigue and fracture analysis. Nevertheless, the variance in service life regardless of constant conditions is a well-known observation in the literature [47].

Structural Fatigue and Fracture Analysis

The actuators failed at 4.5 mm, 13 mm, and 15 mm the nearest sphere base in the unprocessed base material and not in the HAZ as in the tensile tests. The fracture surfaces of all three actuators reveal a consistent fracture

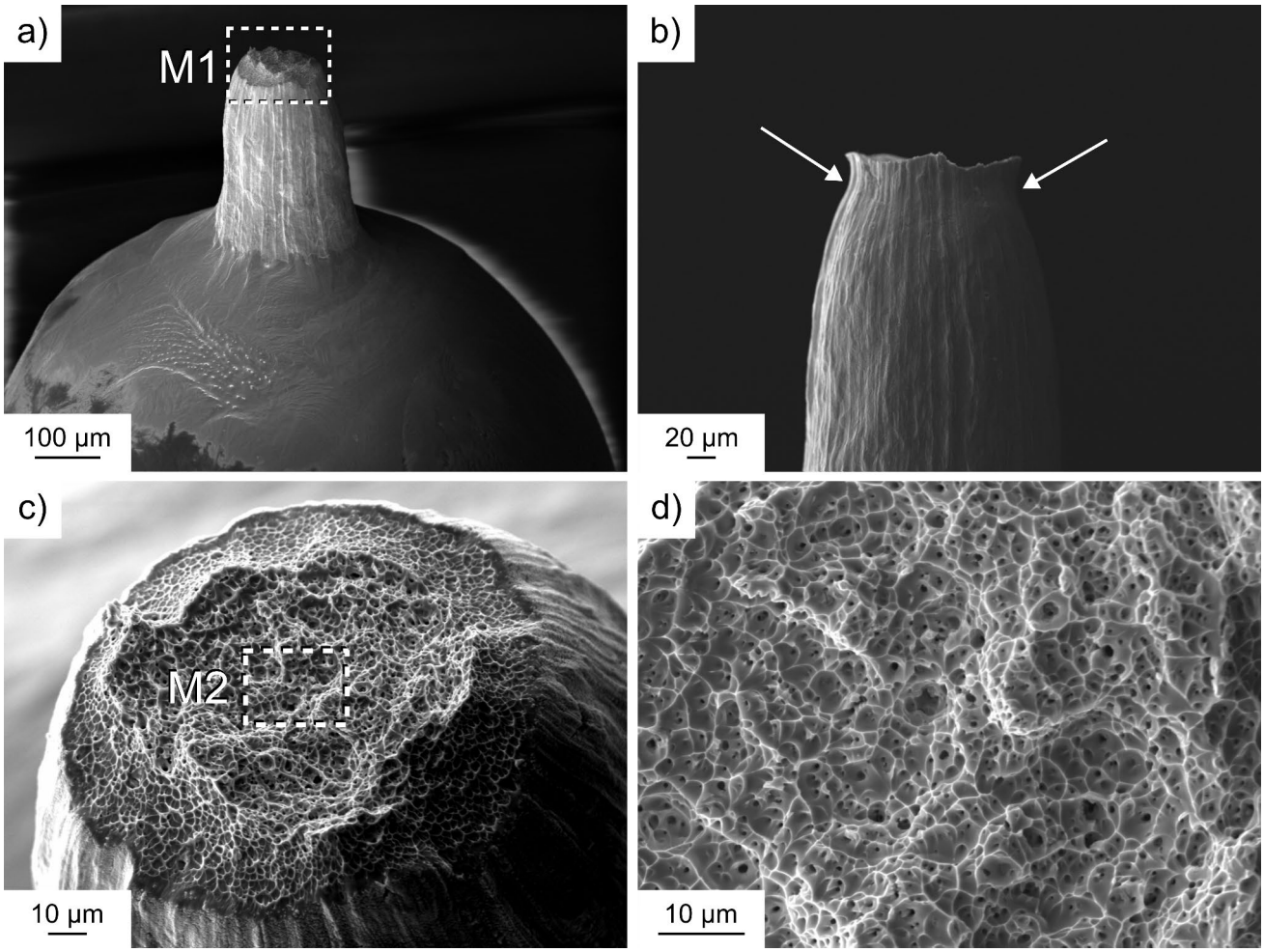

Fig. 6 SEM images of fracture surfaces after tensile testing: **a** fractured wire with manufactured sphere at the bottom, **b** corresponding fracture surface of the wire showing necking with a cup and cone fracture, **c** magnified section M1 of the fracture surface, featuring an internal raised circle and an obliquely lowered external ring, and **d** magnified section M2 showing a dimple fracture

appearance, despite the significantly different service life. Figure 8a shows an example of the fracture surface of Sample 1, which indicates an apparently brittle failure. A semi-circular, inclined surface can be recognized in the bottom area of the fracture surface, which tapers to the edge of the wire. The remaining fracture in Fig. 8b shows a surface with a rough, dimpel-like structure. Figure 8c and d presents magnified images highlighting several small cracks and two larger macroscopic cracks. Crack initiation is primarily observed at or around the wire's surface grooves, which result from the wire drawing process during manufacturing. The macroscopic cracks seem to grow into the interior of the material. No further crack initiation points could be detected within the analysis. Indicators suggesting that laser processing was the cause of the failure were not identified in the inspected samples.

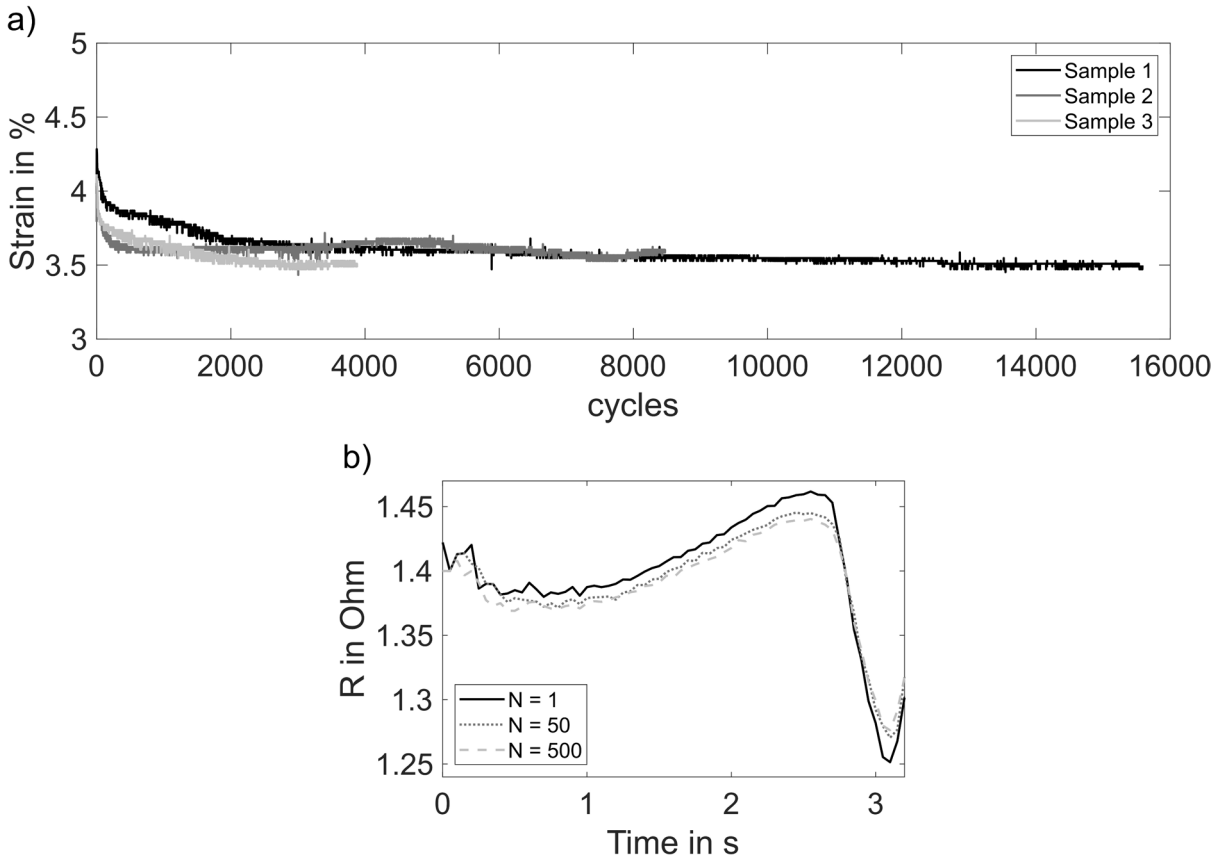

Fig. 7 Fatigue life testing: **a** stress over cycles for three manufactured PCB sphere actuators and **b** resistance profiles while heating of Sample 1 at cycle number $N = 1$, 50, and 500

Conclusion

The presented study demonstrates that the laser-based temperature-controlled production of fused sphere actuators represents a practical integration solution for actuator applications. It was shown that actuators manufactured in this manner have a high degree of reproducibility in terms of mechanical properties and transformation temperatures. The laser processing causes a reduced tensile strength of approximately 942 MPa due to the grain coarsening in the HAZ, which is however entirely sufficient for actuator applications and represents a robust connector for system integration. The functional properties do not show irregularities that can be attributed to the laser processing, which is to be expected since the spheres produced only serve as anchorage and due to the selectively controlled processing, the modified area is minimized. Furthermore, this small part has only a low to no noteworthy contribution to the overall actuator stroke and additionally transforms at significantly increased temperatures. The fracture analysis of the cycled actuators shows cracks that have propagated into the material starting on the wire surface and are responsible for the failure. Future work with optimized wire surfaces is required to further investigate the influence of laser processing in terms of structural fatigue.

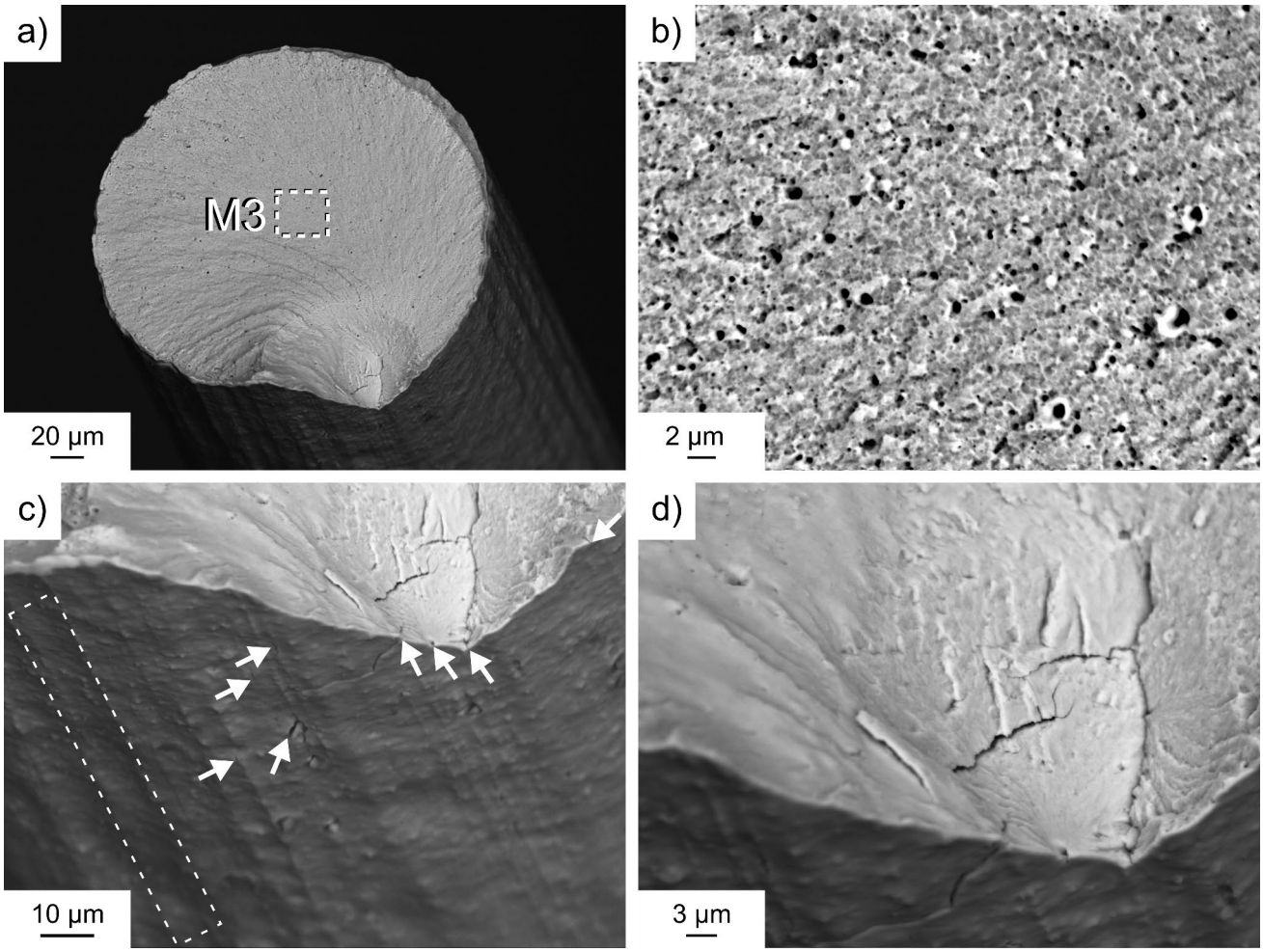

Fig. 8 SEM images of fractured Sample 2: **a** overview of the fracture surface, **b** magnified section M3 of the fracture surface featuring a rough structure, and **c** white arrows indicating cracks at defects on the wire surface as a result of the drawing grooves (marked area). **d** Higher-magnification fractograph of the sample shown in **c**, featuring two small cracks, which have propagated into the wire

Funding Open Access funding enabled and organized by Projekt DEAL. The authors acknowledge funding from the Federal Ministry for Economic Affairs and Climate Action within a Central Innovation Program for Small- and Medium-Sized Enterprises (SMEs) through Projects KK5055205SU1 and KK5251301SU1, as well as funding from the Deutsche Forschungsgemeinschaft (DFG) through Project 498172553. Open Access funding enabled and organized by Projekt DEAL.

Declarations

Conflict of interest The authors declare no competing interests.

References

1. Stöckel D (1990) Shape memory actuators for automotive applications. Mater Des. https://doi.org/10.1016/0261-3069(90)90013-A
2. Gheorghita V, Gümpel P, Chiru A, Strittmatter J (2013) Future applications of NiTi-alloys in automotive safety systems. Int J Automot Technol. https://doi.org/10.1007/s12239-014-0049-z
3. Chau E, Friend CM, Allen DM, Hora J, Webster JR (2006) A technical and economic appraisal of shape memory alloys for aerospace applications. Mater Sci Eng A 438–440:589–592. https://doi.org/10.1016/j.msea.2006.02.201
4. Swain B, Mantry S, Mohapatra SS, Mishra SC, Behera A (2022) Investigation of tribological behavior of plasma sprayed NiTi coating for aerospace application. J Therm Spray Technol 31(8):2342–2369. https://doi.org/10.1007/s11666-022-01452-7

5. Ashbli S, Menzemer C (2019) On the fatigue behavior of nanocrystalline NiTi shape memory alloys: a review. J Nanomed Nanotechnol. https://doi.org/10.35248/2157-7439.19.10.529
6. Maass B, Burow J, Frenzel J, Eggeler G (2009) On the influence of crystal defects on the functional stability of NiTi based shape memory alloys. In: ESOMAT 2009—8th European symposium on martensitic transformations, Prague, Czech Republic, 7–11 September 2009. EDP Sciences, Les Ulis. https://doi.org/10.1051/esomat/200902022
7. Chluba C, Ge W, Dankwort T, Bechtold C, de Miranda RL, Kienle L, Wuttig M, Quandt E (2016) Effect of crystallographic compatibility and grain size on the functional fatigue of sputtered TiNiCuCo thin films. Philos Trans A. https://doi.org/10.1098/rsta.2015.0311
8. Frenzel J, Burow JA, Payton EJ, Rezanka S, Eggeler G (2011) Improvement of NiTi shape memory actuator performance through ultra-fine grained and nanocrystalline microstructures. Adv Eng Mater 13(4):256–268. https://doi.org/10.1002/adem.201000285
9. Burow J, Prokofiev E, Somsen C, Frenzel J, Valiev R, Eggeler GF (2008) Martensitic transformations and functional stability in ultra-fine grained NiTi shape memory alloys. MSF 584–586:852–857. https://doi.org/10.4028/www.scientific.net/MSF.584-586.852
10. Sadrnezhaad SK, Nemati NH, Bagheri R (2009) Improved adhesion of NiTi wire to silicone matrix for smart composite medical applications. Mater Des 30(9):3667–3672. https://doi.org/10.1016/j.matdes.2009.02.016
11. Eyer P, Dittus J, Trauth A, Coutandin S, Fleischer J, Weidenmann KA (2021) Improvement of the adhesion in functional NiTi wire/polymer composites made by additive manufacturing. Compos Struct 275:114455. https://doi.org/10.1016/j.compstruct.2021.114455
12. Niccoli F, Alfano M, Bruno L, Furgiuele F, Maletta C (2014) Mechanical and functional properties of nickel titanium adhesively bonded joints. J Mater Eng Perform 23(7):2385–2390. https://doi.org/10.1007/s11665-014-0890-2
13. Man HC, Zhao NQ (2006) Enhancing the adhesive bonding strength of NiTi shape memory alloys by laser gas nitriding and selective etching. Appl Surf Sci 253(3):1595–1600. https://doi.org/10.1016/j.apsusc.2006.02.057
14. Schuleit M, Becher M, Franke F, Maaß B, Esen C (2020) Development of form-fit connection for NiTi shape memory wire actuators using laser processing. Procedia CIRP 94:546–550. https://doi.org/10.1016/j.procir.2020.09.180
15. Mehrpouya M, Gisario A, Elahinia M (2018) Laser welding of NiTi shape memory alloy: a review. J Manuf Process 31:162–186. https://doi.org/10.1016/j.jmapro.2017.11.011
16. Mehrpouya M, Gisario A, Broggiato GB, Puopolo M, Vesco S, Barletta M (2019) Effect of welding parameters on functionality of dissimilar laser-welded NiTi superelastic (SE) to shape memory effect (SME) wires. Int J Adv Manuf Technol 103(1–4):1593–1601. https://doi.org/10.1007/s00170-019-03514-7
17. Schuleit M, Theren B, Maaß B, Kuhlenkötter B, Esen C (2022) Micro laser welding of NiTi shape memory wires and printed circuit boards. In: Proceedings of ASME 2022 conference on smart materials, adaptive structures and intelligent systems (SMASIS 2022), 12–14 September 2022, Dearborn, Michigan. The American Society of Mechanical Engineers, New York. https://doi.org/10.1115/SMASIS2022-90970
18. Gugel H, Schuermann A, Theisen W (2008) Laser welding of NiTi wires. Mater Sci Eng A 481–482:668–671. https://doi.org/10.1016/j.msea.2006.11.179
19. Falvo A, Furgiuele FM, Maletta C (2005) Laser welding of a NiTi alloy: mechanical and shape memory behaviour. Mater Sci Eng A 412(1–2):235–240. https://doi.org/10.1016/j.msea.2005.08.209
20. Zeng Z, Yang M, Oliveira JP, Song D, Peng B (2016) Laser welding of NiTi shape memory alloy wires and tubes for multifunctional design applications. Smart Mater Struct 25(8):85001. https://doi.org/10.1088/0964-1726/25/8/085001
21. Bernauer CJ, Zapata A, Kick L, Weiss T, Sigl ME, Zaeh MF (2022) Pyrometry-based closed-loop control of the melt pool temperature in Laser Metal Deposition with coaxial wire feeding. Procedia CIRP 111:296–301. https://doi.org/10.1016/j.procir.2022.08.025
22. Carcel B, Sampedro J, Perez I, Fernandez E, Ramos JA (2010) Improved laser metal deposition (LMD) of nickel base superalloys by pyrometry process control. In: Dreischuh T, Atanasov PA, Sabotinov NV (eds) XVIII international symposium on gas flow, chemical lasers, and high-power lasers, Sofia, Bulgaria, 30 August 2010. SPIE, pp 775123–775123-9. https://doi.org/10.1117/12.878749
23. Salehi D, Brandt M (2006) Melt pool temperature control using LabVIEW in Nd:YAG laser blown powder cladding process. Int J Adv Manuf Technol 29(3–4):273–278. https://doi.org/10.1007/s00170-005-2514-3
24. Song L, Bagavath-Singh V, Dutta B, Mazumder J (2012) Control of melt pool temperature and deposition height during direct metal deposition process. Int J Adv Manuf Technol 58(1–4):247–256. https://doi.org/10.1007/s00170-011-3395-2
25. Phillips FR, Wheeler RW, Geltmacher AB, Lagoudas DC (2019) Evolution of internal damage during actuation fatigue in shape memory alloys. Int J Fatigue 124:315–327. https://doi.org/10.1016/j.ijfatigue.2018.12.019
26. Ramaiah KV, Saikrishna CN, Ranganath VR, Buravalla V, Bhaumik SK (2011) Fracture of thermally activated NiTi shape memory alloy wires. Mater Sci Eng A 528(16–17):5502–5510. https://doi.org/10.1016/j.msea.2011.03.070
27. Bigeon MJ, Morin M (1996) Thermomechanical study of the stress assisted two way memory effect fatigue in TiNi and CuZnAl wires. Scr Mater 35(12):1373–1378. https://doi.org/10.1016/S1359-6462(96)00228-X
28. Calhoun C, Wheeler R, Baxevanis T, Lagoudas DC (2015) Actuation fatigue life prediction of shape memory alloys under the constant-stress loading condition. Scr Mater 95:58–61. https://doi.org/10.1016/j.scriptamat.2014.10.005
29. Murray JL (ed) (1987) Phase diagrams of binary titanium alloys. Monograph series on alloy phase diagrams, 2nd edn, vol 2. ASM International, Metals Park
30. Grossmann C, Frenzel J, Sampath V, Depka T, Oppenkowski A, Somsen C, Neuking K, Theisen W, Eggeler G (2008) Processing and property assessment of NiTi and NiTiCu shape memory actuator springs. Mater Wissenschaft Werkst 39(8):499–510. https://doi.org/10.1002/mawe.200800271
31. Frenzel J, George EP, Dlouhy A, Somsen C, Wagner M-X, Eggeler G (2010) Influence of Ni on martensitic phase transformations in NiTi shape memory alloys. Acta Mater 58(9):3444–3458. https://doi.org/10.1016/j.actamat.2010.02.019
32. Waitz T, Kazykhanov V, Karnthaler HP (2004) Martensitic phase transformations in nanocrystalline NiTi studied by TEM. Acta Mater 52(1):137–147. https://doi.org/10.1016/j.actamat.2003.08.036
33. Mentz J, Frenzel J, Wagner MF-X, Neuking K, Eggeler G, Buchkremer HP, Stöver D (2008) Powder metallurgical processing of NiTi shape memory alloys with elevated transformation temperatures. Mater Sci Eng A 491(1–2):270–278. https://doi.org/10.1016/j.msea.2008.01.084

34. Robertson SW, Pelton AR, Ritchie RO (2012) Mechanical fatigue and fracture of Nitinol. Int Mater Rev 57(1):1–37. https://doi.org/10.1179/1743280411Y.0000000009
35. Frenzel J (2020) On the importance of structural and functional fatigue in shape memory technology. Shape Mem Superelast 6(2):213–222. https://doi.org/10.1007/s40830-020-00281-3
36. Theren B, Heß P, Bracke S, Kuhlenkötter B (2022) The development and verification of a simulation model of shape-memory alloy wires for strain prediction. Crystals 12(8):1121. https://doi.org/10.3390/cryst12081121
37. Calhoun C, Lagoudas D (2011) Microstructural effects on actuation fatigue life of Ni-rich NiTi shape memory alloy actuators. In: 52nd AIAA/ASME/ASCE/AHS/ASC structures, structural dynamics and materials conference, 2011, Denver, Colorado. American Institute of Aeronautics and Astronautics, Reston. https://doi.org/10.2514/6.2011-2106
38. Grossmann C, Frenzel J, Sampath V, Depka T, Eggeler G (2009) Elementary transformation and deformation processes and the cyclic stability of NiTi and NiTiCu shape memory spring actuators. Metall Mater Trans A 40(11):2530–2544. https://doi.org/10.1007/s11661-009-9958-2
39. Lagoudas DC, Miller DA, Rong L, Kumar PK (2009) Thermomechanical fatigue of shape memory alloys. Smart Mater Struct 18(8):85021. https://doi.org/10.1088/0964-1726/18/8/085021
40. LePage WS, Shaw JA, Daly SH (2021) Effects of texture on the functional and structural fatigue of a NiTi shape memory alloy. Int J Solids Struct 221:150–164. https://doi.org/10.1016/j.ijsolstr.2020.09.022
41. Sgambitterra E, Magarò P, Niccoli F, Furgiuele F, Maletta C (2021) Fatigue crack growth in austenitic and martensitic NiTi: modeling and experiments. Shape Mem Superelast 7(2):250–261. https://doi.org/10.1007/s40830-021-00327-0
42. Eggeler G, Hornbogen E, Yawny A, Heckmann A, Wagner M (2004) Structural and functional fatigue of NiTi shape memory alloys. Mater Sci Eng A 378(1–2):24–33. https://doi.org/10.1016/j.msea.2003.10.327
43. Casati R, Saghafi F, Biffi CA, Vedani M, Tuissi A (2017) Improved functional properties and efficiencies of Nitinol wires under high-performance shape memory effect (HP-SME). J Mater Eng Perform 26(10):4964–4969. https://doi.org/10.1007/s11665-017-2927-9
44. Lynch B, Jiang X-X, Ellery A, Nitzsche F (2016) Characterization, modeling, and control of Ni–Ti shape memory alloy based on electrical resistance feedback. J Intell Mater Syst Struct 27(18):2489–2507. https://doi.org/10.1177/1045389X16633764
45. Costanza G, Paoloni S, Tata ME (2014) IR thermography and resistivity investigations on Ni–Ti shape memory alloy. KEM 605:23–26. https://doi.org/10.4028/www.scientific.net/KEM.605.23
46. Uchil J, Mahesh KK, Ganesh Kumara K (2002) Electrical resistivity and strain recovery studies on the effect of thermal cycling under constant stress on R-phase in NiTi shape memory alloy. Physica B 324(1):419–428. https://doi.org/10.1016/S0921-4526(02)01462-X
47. Sgambitterra E, Magarò P, Niccoli F, Renzo D, Maletta C (2019) Low-to-high cycle fatigue properties of a NiTi shape memory alloy. Procedia Struct Integr 18:908–913. https://doi.org/10.1016/j.prostr.2019.08.242